NeuroImage 195 (2019) 463–474

Contents lists available at ScienceDirect

NeuroImage

journal homepage: www.elsevier.com/locate/neuroimage

Quantitative phase contrast MRI of penetrating arteries in centrum semiovale at 7T

Xiaopeng Zong *, Weili Lin

Department of Radiology and Biomedical Research Imaging Center, University of North Carolina at Chapel Hill, Chapel Hill, NC, 27599, USA

ARTICLE INFO

Keywords:
Partial volume
Penetrating artery
Flow quantification
Phase contrast MRI
Age dependence
Small vessel disease

ABSTRACT

Pathological changes of penetrating arteries (PA) within the centrum semiovale is an important contributing factor of cerebral small vessel disease (SVD). However, quantitative characterization of the PAs remains challenging due to their sub-voxel sizes. Here, we proposed a Model-based Analysis of Complex Difference images (MACD) of phase contrast MRI capable of measuring the mean velocities (v_{mean}), diameters (D), and volume flow rates (VFR) of PAs without contamination from neighboring static tissues at 7 T.

Simulation, phantom and *in vivo* studies were performed to evaluate the reproducibility and errors of the proposed method. For comparison, a Model-based Analysis of Phase difference images (MAP) was also carried out in the simulation. The proposed MACD analysis approach was applied *in vivo* to study the age dependence of PA properties in healthy subjects between 21 and 55 years old.

Simulation showed that our proposed MACD approach yielded smaller errors than MAP, with errors increasing at lower velocities and diameters for both methods. In the phantom study, errors of the MACD-derived v_{mean}, D, and VFR were $\leq$20% of their true values when $v_{mean} \geq$ 1cm/s and similar at different spatial resolutions. On the other hand, errors of the uncorrected apparent velocities were 24–60% and depended strongly on voxel size. The MACD errors linearly increased with the angle (α) between the vessel and slice normal direction at $\alpha \leq 2^\circ$ but remained almost constant at larger α. Results of the *in vivo* studies showed that the coefficients of repeatability for v_{mean}, D, and VFR for PAs with $\alpha = 0^\circ$ were 0.67 cm/s, 0.060 mm, and 0.067 mm^3/s, respectively. No significant age dependence was found for the number, v_{mean}, D, and VFR of PAs. The mean v_{mean}, D, and VFR over all PAs with $\alpha = 0^\circ$ were 1.79 ± 0.62 cm/s, 0.17 ± 0.05 mm, and 0.36 ± 0.18 mm^3/s, respectively.

Quantitative measurements of PAs with the MACD method may serve as a useful tool for illuminating the vascular pathology in cerebral SVD.

1. Introduction

Pathological changes of penetrating arteries (PAs) within deep white matter (WM) of the centrum semiovale (CSO) play a critical role in cerebral small vessel disease (SVD) (Fisher, 1968; Jorgensen et al., 2018; Pantoni, 2010; Snyder et al., 2015; van Swieten et al., 1991; Wardlaw et al., 2001). Narrowing or occlusion of PAs could lead to focal ischemia (Bernbaum et al., 2015) whereas leakage of the blood brain barrier of PAs could result in accumulation of toxic components in surrounding tissues (Fisher, 1968; Montagne et al., 2018; Wardlaw et al., 2001). Thus, the ability to non-invasively measure the morphological and functional properties of PAs should facilitate delineating these underlying pathologies, which may in turn allow the development of effective treatment strategies for small vessel diseases.

Phase contrast (PC) MRI is an established method for measuring blood flow in large arteries such as internal carotid and basilar arteries (ten Dam et al., 2007; van der Veen et al., 2015). More recently, the increased spatial resolution at 7T has enabled measurements of the velocity of lenticulostriate arteries in the basal ganglia (Bouvy et al., 2016; Kang et al., 2016; Schnerr et al., 2017). However, the majority of PAs in the CSO have diameters less than 100 μm (Furuta et al., 1991; Miao et al., 2004), making it difficult to assess their structural and functional properties without severe partial volume effects using MRI (Geurts et al., 2018b). Different image analysis strategies have been proposed to account for partial volume effects for flow quantification of small intracranial vessels. For example, Tang et al. proposed to correct the volume

* Corresponding author. Department of Radiology and Biomedical Research Imaging Center, University of North Carolina at Chapel Hill, CB#7515, Chapel Hill, NC, 27599, USA.
E-mail address: xiaopeng_zong@med.unc.edu (X. Zong).

https://doi.org/10.1016/j.neuroimage.2019.03.059
Received 29 December 2018; Received in revised form 27 February 2019; Accepted 25 March 2019
Available online 29 March 2019

flow rate in voxels near the lumen boundary by the ratio of image intensity in such voxels to that of voxels fully occupied by blood (Tang et al., 1995). However, this method is not applicable to PAs since no voxel fully occupied by blood exists. Furthermore, the method did not consider the difference in flow-induced signal enhancement between spins in boundary and fully occupied voxels which exists because of their difference in velocities. Hamilton proposed to fit a circle to a pair of velocity-encoded data in the complex plane (Hamilton, 1994). However, this method did not consider the blurring effect due to finite k-space sampling. Lagerstrand et al. proposed to correct the partial volume effects using a calibration curve obtained from a separate measurement on a flow phantom with similar relaxation and flow properties (Lagerstrand et al., 2002). Due to the requirement of a calibration curve, this method cannot be readily applied to *in vivo* studies with unknown flow rates. Hoogeveen et al. proposed Model-based Analysis of Phase difference images (MAP) to correct for partial volume effects (Hoogeveen et al., 1999), where the model image accounts for blurring due to the limited spatial resolution and flow-induced signal enhancement. However, the accuracy of the MAP approach for sub-voxel vessels was not systematically evaluated, and the error for volume flow rate (VFR) already reached ~45% when the voxel dimension was only slightly greater than (1.1 times) the vessel diameter. Furthermore, a two-pool model was assumed in calculating the model phase images, which may not be applicable to PAs due to the presence of surrounding perivascular spaces (PVSs), vessel wall, and WM with different MR properties. Assuming a two-compartment model, Nitz et al. derived an analytical solution to correct partial volume effects in measuring the flow of cerebral spinal fluid (Nitz et al., 1992). However, in addition to the potential errors introduced by the two-compartment model, reference regions fully occupied by flowing spins were needed, and flow-induced signal enhancement was not considered.

In order to mitigate the limitations of the aforementioned approaches, we propose a new approach for measuring diameters and flow velocities of PAs based on Model-based Analysis of Complex Difference images (MACD) in PC MRI. Complex difference eliminates the static tissue contributions in images. Therefore, our approach is applicable even when there are multiple static tissue compartments. Furthermore, compared to the MAP method, the MACD approach utilizes both the phase and magnitude changes induced by flow, leading to improved precision of fitted parameters. Detailed simulation, phantom studies, and *in vivo* evaluation of the precision and accuracy of our proposed approach were conducted. The developed method was then applied to study the potential age-related changes of PAs in 44 healthy subjects between 21 and 55 years old. Note that a list of abbreviations used throughout this manuscript is provided in the supporting materials.

2. Methods and materials

2.1. Theory

The proposed MACD approach consists of fitting the experimentally measured complex difference images with a model complex difference image to derive PA properties. The model image was calculated by convoluting a true complex difference image with a point spread function (PSF) to account for the finite spatial resolution of the MRI images. Fig. 1 shows the flow-chart of the proposed MACD method.

The PA was assumed to be perpendicular to the imaging plane. Due to the non-Newtonian property of human blood, the velocity (v) within the

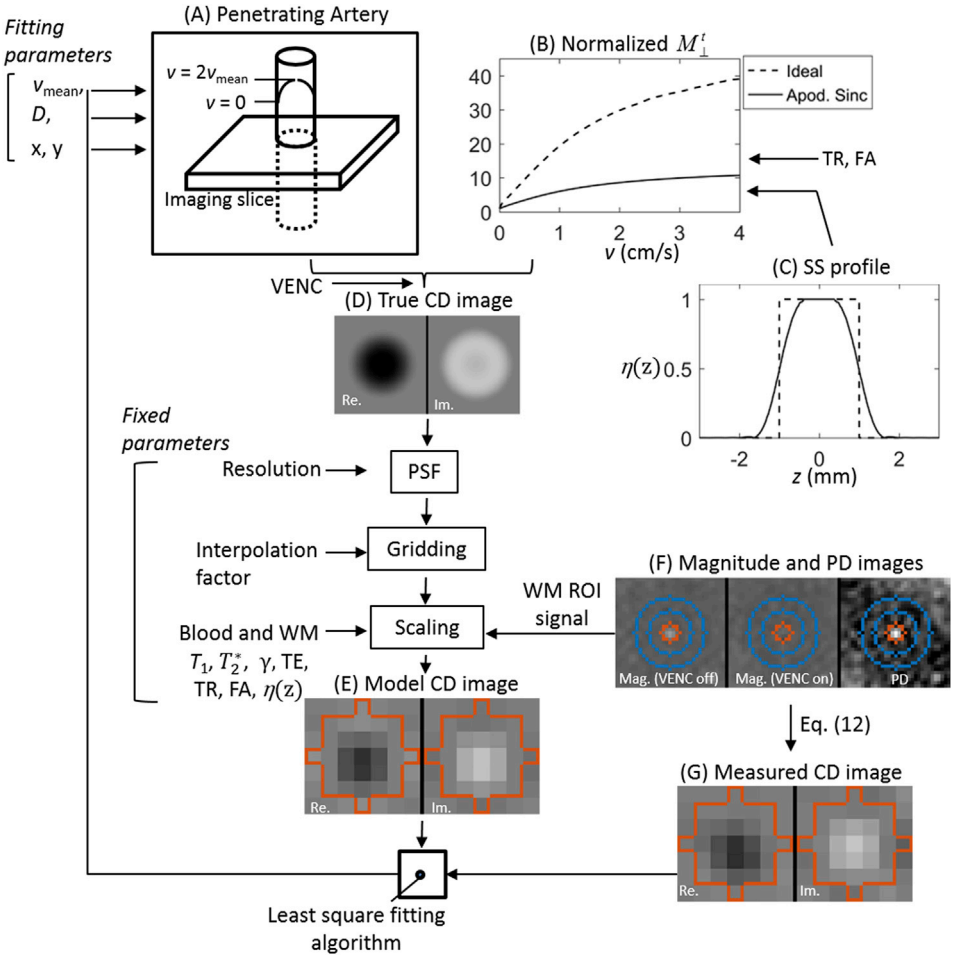

Fig. 1. Flow chart of the MACD method. (A) A penetrating artery with an assumed flow velocity (v) pattern and perpendicular to imaging slice. (B) Total transverse magnetization ($M_\perp^t$) versus v for two slice selection (SS) profiles. $M_\perp^t$ is normalized by its value at $v = 0$. (C) SS profile of the experimental apodized sinc and ideal pulses. (D) True CD images (both real (Re) and imagery (Im) parts) calculated from the v spatial pattern in (A) and the $M_\perp^t$ versus v curve in (B). (E) Model CD image after convolution, gridding, and scaling operations. The scaling factor was obtained from the WM ROI shown in (F). (F) Representative magnitude and phase difference (PD) images after detrending. The ROIs for MACD analysis (orange) and WM background (blue) are also shown. (G) Measured CD image calculated from (F) with Eq. (10). See the text in the Theory section for further details.

PA does not follow the laminar pattern as described by a parabolic function of the distance from the vessel axis:

$$v(x,y) = 2v_{mean}\left[1 - 4\left(x^2 + y^2\right)/D^2\right], \tag{1}$$

where v_{mean} is the mean velocities and D is the lumen diameter. Instead, the velocity profile is blunter than a parabola, i.e. the velocities are higher than a parabola except for at $(x^2 + y^2) = 0$ and $(x^2 + y^2) = D^2/4$ where they are equal between the two profiles. The following profile obtained by averaging over multiple experiments will be adopted to represent the velocity profile in PAs (Koutsiaris, 2009):

$$v(x,y) = 1.49v_{mean}\left[1 - 2.32\left(x^2 + y^2\right)/D^2\right]\left[1 - 4^{11}\left(x^2 + y^2\right)^{11}\Big/D^{22}\right] \tag{2}$$

Errors caused by the mismatch between the assumed and true profiles will be evaluated by simulation.

Because spins with different velocities have different spin history while traveling through an imaging slice, the transverse magnetization integrated along the slice direction ($M^t_\perp$) is velocity dependent. The functional form of $M^t_\perp(v)$ (Fig. 1(B)) can be obtained using Bloch simulation for given TR, flip angle (FA), and RF slice selection (SS) profile ($\eta(z)$, Fig. 1(C)), as described in the Appendix (Eq. (A1) and (A2)). From $M^t_\perp(v)$ and the assumed velocity pattern (Eq. (1) or (2)), image $M^t_\perp(x,y)$ can be calculated. The phase of the $M^t_\perp(x,y)$ images can be modulated by applying a velocity encoding gradient. The complex difference of $M^t_\perp(x,y)$ (Fig. 1(D)) with and without the velocity encoding gradient removes the static spin contributions in the image. The complex difference is then convoluted with sinc-shaped PSFs, gridded to match the voxel size of measured complex difference images, and converted from magnetization to image intensity by multiplying a scaling factor (A), which produces the final model complex difference image (Fig. 1(E)) as:

$$CD(x,y) = A\left\{M^t_\perp(v(x,y))\cdot\left(e^{i\pi v(x,y)/VENC} - 1\right)\right\} \otimes \mathrm{PSF}(x,y)\cdot\Pi(x,y), \tag{3}$$

where $\Pi(x,y)$ is the gridding function, and $M^t_\perp(x,y) = 0$ when $(x^2 + y^2) > D^2/4$. $\mathrm{PSF}(x,y)$ is related to the largest measured k-space coordinates along x- and y-axes ($k_{x,\max}$ and $k_{y,\max}$) as

$$\mathrm{PSF}(x,y) = k_{x,\max}k_{y,\max}\left[\mathrm{sinc}\left(k_{x,\max}x\right)\mathrm{sinc}\left(k_{y,\max}y\right)\right]/\pi^2. \tag{4}$$

The scaling factor A can be estimated from the mean signal (S_{wm}) of a nearby WM ROI (blue ring in Fig. 1(F)) as

$$A = \gamma S_{\mathrm{wm}}\Big/M^t_{\perp,\mathrm{wm}}, \tag{5}$$

where γ is the blood-WM water partition coefficient ($\gamma = 1.05$ in healthy adult brain (Herscovitch and Raichle, 1985)) and $M^t_{\perp,wm}$ is the transverse magnetization of WM integrated along z. The equation for calculating $M^t_{\perp,wm}$ is given in the Appendix (Eq. (A3)).

Although the proposed MACD method still requires the signal from adjacent WM for calculating the factor A, the model complex difference image (Eq. (3)) only contains a single pool, as opposed to two-pool models proposed by others (Hoogeveen et al., 1999; Nitz et al., 1992; Tang et al., 1995). Therefore, our method does not entail an appropriate modeling of static tissues in close proximity to the PAs, and is therefore more suitable for PAs where signals from nearby static tissues with unknown composition can overlap with PAs due to the limited spatial resolution. The WM ROI for calculating A can be chosen as surrounding voxels fully occupied by WM, such as those within the blue ring in Fig. 1(F), thus avoiding the partial volume effects of unknown tissue compositions.

In contrast to MACD, the MAP method fits the measured phase difference image with a model image calculated from

$$\varphi(x,y) = \arg\left(I_{\mathrm{on}}(x,y)\cdot I^*_{\mathrm{off}}(x,y)\right), \tag{6}$$

where I_{on} and I_{off} are the two-pool model complex images with and without velocity encoding gradients, respectively, and are given by

$$I_{on}(x,y) = A\cdot\left\{M^t_\perp(v(x,y))\cdot e^{i\pi v(x,y)/VENC} + M^t_{\perp,\mathrm{wm}}H\left(2\sqrt{x^2+y^2} - D\right)\Big/\gamma\right\} \otimes \mathrm{PSF}(x,y)\cdot\Pi(x,y) \tag{7}$$

and

$$I_{off}(x,y) = A\cdot\left\{M^t_\perp(v(x,y)) + M^t_{\perp,\mathrm{wm}}H\left(2\sqrt{x^2+y^2} - D\right)\Big/\gamma\right\} \otimes \mathrm{PSF}(x,y)\cdot\Pi(x,y), \tag{8}$$

where $H(x)$ is the Heaviside step function.

Experimentally, complex difference can be calculated directly from measured $I_{\mathrm{on}}(x,y)$ and $I_{\mathrm{off}}(x,y)$ as

$$CD(x,y) = I_{\mathrm{on}}(x,y) - I_{\mathrm{off}}(x,y). \tag{9}$$

Alternatively, when I_{off} has a zero phase (after removing constant offset and slow spatial variations which can be induced by eddy-current), Eq. (9) can be written as

$$CD(x,y) = |I_{\mathrm{on}}(x,y)|\exp(i\varphi(x,y)) - |I_{\mathrm{off}}(x,y)|, \tag{10}$$

where φ is the phase difference resulting from the presence of velocity encoding gradients. For phased array coils, phase difference is calculated as

$$\varphi(x,y) = \arg\left(\sum_c I_{\mathrm{on},c}(x,y)\cdot I^*_{\mathrm{off},c}(x,y)\right), \tag{11}$$

where c denotes the coil index (Bernstein et al., 1994). Equation (10) is more straightforward to calculate than Eq. (9) for phased array coils since there is no need to reconstruct combined phase images for I_{on} and I_{off}. However, the assumption of zero phase may not hold for I_{off} if negative Gibbs ringing signal from the vessel exceeds the signal of surrounding tissue. In such a case, Eq. (10) is no longer valid and complex difference image should be calculated from Eq. (9). The presence of phase oscillations caused by Gibbs ringing can be visually identified in uncombined phase images of individual coils.

Before calculating the complex difference images using Eq. (10), the phase difference and magnitude images should be detrended to remove slow spatial variations in the background near PAs. For this purpose, we fitted the pixel values in the ring-shaped WM ROI using a second order polynomial:

$$B(x,y) = c_0 + c_1x + c_2y + c_3x^2 + c_4y^2 + c_5xy \tag{12}$$

The fitted functions were then subtracted from the original images to ensure homogeneous background. In case of the magnitude images, a constant equal to the means within the ring-shaped WM ROI were added back to the subtracted images so that only spatial variations were removed.

The MACD method estimates v_{mean}, D, and VFR (which is $\pi D^2 v_{\mathrm{mean}}/4$) by nonlinear least-square fitting of the experimentally obtained complex difference images with model images calculated from Eq. (3) in a circular ROI enclosing a given vessel (the orange circle in Fig. 1(F)), with v_{mean}, D, and vessel position in the ROI as free parameters. In contrast, the MAP method fits the phase difference images with the model image calculated from Eq. (6), as proposed by Hoogeveen et al. (1999). Note that the v_{mean}, D parameters are implicitly included in Eqs. (3) and (6) via their effects on $v(x,y)$.

It is important to note that in order to ensure accuracy of the MACD fitting results, the PC MRI sequence should acquire images with and without the velocity encoding gradient (Fig. 2(A)), which will be referred to as one-sided encoding, instead of acquiring two images with opposite

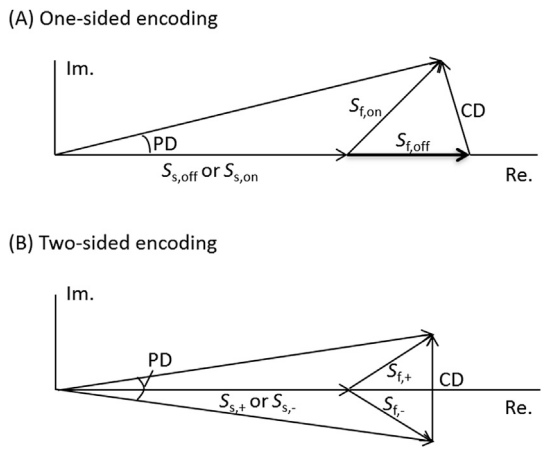

Fig. 2. Graphic representations of the stationary and flowing spin signals, complex difference (CD), and phase difference (PD) in the complex plane in scans with (A) one-sided and (B) two-sided velocity encoding gradients. The subscript s and f denote stationary and flowing spins, respectively. In (A), on and off denote the gradients on and off. In (B), + and - denote the opposite polarities of the gradients.

polarities of the gradients (two-sided encoding; Fig. 2(B)). In the two-sided encoding, the real part of the complex difference image is always zero and the velocity encoding phase information is lost. As a result, velocity mainly affects the overall intensity of the complex difference image. Its effect then becomes similar to that of the vessel diameter. Therefore, the errors of the fitted v_{mean} and D values become highly correlated and sensitive to noise. In contrast, in the one-sided encoding, the phase is mostly determined by v_{mean}, while the signal intensity is determined by both v_{mean} and D. Therefore, different information on the complex difference images are utilized to optimize v_{mean} and D during fitting, resulting in smaller measurement errors.

2.2. Simulation

We carried out simulations to evaluate errors resulting from noise as well as model parameters for both the MACD and MAP approaches. The following three simulations were carried out.

Simulation 1: The goal was to study the noise-induced random and systematic errors, including their dependences on true v_{mean} and D, and to compare errors between MACD and MAP. Complex images were simulated by adding complex Gaussian white noise to Eqs. (7) and (8), assuming a two-compartment (WM + blood) model. The values of the model parameters are listed in Table 1, which match closely with *in vivo* experimental conditions at 7T. The images were sampled to a voxel size of 0.156×0.156 mm^2 (half the acquired voxel size) and had a matrix size of 23×23. We assumed the blunted parabolic velocity profile as given by Eq. (2). The blood and WM T_1 values were taken from (Rooney et al., 2007). The blood and WM T_2^* values were measured at internal carotid arteries (ICA) and WM ROIs, respectively, in a single young healthy subject (age 21, male) using a multi-echo gradient echo sequence. γ value is from (Herscovitch and Raichle, 1985).

The SD of the Gaussian noise was chosen such that the SNR of the WM image intensity matched with the WM SNR in *in vivo* Study 1 (SNR ~ 27). Nineteen true D and 20 true v_{mean} values were simulated. The diameters were in the range of 112–353 μm, which corresponds to partial volume fractions (PVF) of 10–100% in a step size of 5%. The PVF was calculated as $\mathrm{PVF} = \pi \cdot D^2/(4\Delta_x\Delta_y)$, where $\Delta_x \times \Delta_y$ is the acquired in-plane voxel size (0.31×0.31 mm^2). True v_{mean} was in the range of 0.1–2 cm/s in a step of 0.1 cm/s. The phase difference images were calculated from the simulated images via Eq. (6). To match the analysis procedure for experimental images, detrending was also performed (although not needed) on the phase difference and magnitude images on a background ROI centered at the vessel and having inner and outer radii of 0.94 and 1.72 mm, respectively. Then, complex difference images were calculated from the detrended images with Eq. (10). They were then fitted with the model images to derive vessel parameters. Only voxels within a circular ROI with a radius of 3 voxels centered at the vessel were included in the fitting.

The fitting procedures were repeated 200 times in each simulation condition with new noise for each repetition to calculate the means and standard deviations (SD) of the fitted v_{mean}, D and VFR over the repetitions. The 200 repetitions would allow estimation of SDs that are within 10% of their true values with 95% confidence (Greenwood and Sandomire, 1950). The SDs and the differences between the means and true values are referred to as the random and systematic errors, respectively, throughout the paper.

Simulation 2: The goal was to evaluate the dependence of the MACD errors on the noise level. Simulated images were generated in the same way as that described in Simulation 1. Two true v_{mean} of 1 and 2 cm/s and two PVF of 20% and 40% were simulated. The SD of the Gaussian noise was adjusted to achieve WM SNRs of 5–40 in a step of 5. The simulated range corresponds to expected SNRs for scan durations ranging from ~10 s–10 min (number of averages ~ 1–64).

Simulation 3: The goal was to evaluate systematic errors of the MACD results due to mismatches in model parameter values adopted during simulation and model fitting. The SNR of the WM signal was the same as that in Simulation 1. The assumed true PVF was 20% and true v_{mean} was 1 cm/s. During simulated image calculation, one of six parameters including blood and WM T_1, blood and WM T_2*, FA, and γ, was set to 80–120% of its value listed in Table 1, in a step of 5%, while the other parameters were set to values listed in Table 1. Alternatively, the flow pattern was assumed to be laminar while keeping the six parameter values the same as in Table 1. During fitting, all parameters have the same values as listed in Table 1.

The convolution in Eqs. (3), (7) and (8) was implemented using finite element calculation with an element width equal to 1/64 of the acquired voxel size. The five central lobes of the sinc function were taken to speed up the calculation, as the errors due to truncation were found to be negligible (Hoogeveen et al., 1999). The convoluted small voxel size images were downsampled by a factor of 32 to produce the final simulated images. The model images were calculated in real-time during fitting. The fitting was carried out with the function "lsqnonlin" in MATLAB (MathWorks, Natick, MA, USA), which returned vessel position in cm, D in mm, and v_{mean} in 10 cm/s when the final step size was less than 10^{-6}. In almost all cases, lsqnonlin returned after less than 100 iterations and took ~15 s on a Windows PC equipped with Intel Core i7-7500U CPU and 16 GB RAM. The initial values for v_{mean} and D were randomly set to 20%–180% of their true values while the initial vessel position matched its true location.

2.3. Phantom experiments

All phantom and *in vivo* experiments were performed on a Siemens 7T human MRI scanner (Siemens Healthineers, Erlangen, Germany) using an

Table 1
Model parameter values in the simulation. Values in the first six columns are also adopted for calculating model CD imaging in MACD of *in vivo* images.

Blood and WM Parameters at 7T						Sequence Parameters in Simulation					
velocity profile	γ	Blood T_1	WM T_1	Blood T_2*	WM T_2*	TE (ms)	TR (ms)	FA	Slice Thickness	VENC (cm/s)	Voxel size (mm^2)
Blunted parabolic	1.05	2.6 s	1.2 s	29 ms	24 ms	15.7	26	45°	2 mm	4	0.3125^2

eight-channel transmit and thirty two-channel receive coil (Nova Medical, Wilmington, MA, USA). No RF shimming was performed during the scan.

Phantom preparation: A flow phantom was constructed to validate the accuracy of the MACD approach and to evaluate its dependence on flow velocity and tilt angle. The phantom consisted of a polyimide thermoset plastic tube with ID = 0.165 mm and OD = 0.305 mm (Neuralynx, Bozeman, MT, USA) penetrating horizontally through a cylindrical plastic cup with ID = 3.5 cm and height = 4.0 cm. Both the cup and tube were filled with tap water. The tube was connected to a 1 ml syringe via a polyethylene PE-10 tube. The syringe was driven by a syringe pump (PHD 2000 Dual Syringe Pump, Harvard Apparatus, Holliston, MA, USA) at constant flow rates to achieve desired v_{mean}.

MRI parameters: Images were acquired with a single slice 2D PC MRI sequence using one-sided velocity encoding gradient. To guide the placement of the imaging slice, the flow phantom was imaged with a 3D GRE sequence. In the 3D images, the tube was visualized as a dark line. Water T_1, needed for calculating the factor A, was measured with a variable TR turbo-spin echo sequence with 9 TR values (Conturo et al., 1987). The sequence was repeated four times to improve accuracy. Because of the B_1 field inhomogeneity at 7T, B_1 maps were obtained at the beginning of the experiment to achieve the desired flip angle at the tube in the imaging slice. The B_1 mapping sequence consisted of a slice-selective pre-saturation pulse followed by a gradient echo imaging sequence. B_1 values were calculated from the intensity ratio with and without applying the pre-saturation pulse. All parameters are provided in columns 2–5 in Table 2.

Two different studies were carried out. Study 1 was designed to study the dependence of the errors of the MACD results on velocity, when the vessel was perpendicular to the imaging slice. The scan was performed at four v_{mean} of 0.8, 1.0, 1.25 and 1.5 cm/s, respectively. Study 2 was designed to study the systematic errors of the MACD results at different tilt angles from the slice normal direction. v_{mean} was set to 1 cm/s and the slice orientation was varied such that the plastic tube formed angles of 0 to 10° from the slice normal direction. The scan under each condition was repeated for 7 to 18 times to improve the precision and evaluate the inter-scan SDs.

Data analysis: Images were reconstructed offline to a voxel size of $0.1563 \times 0.1563\ mm^2$ by zero padding in k-space before inverse Fourier transform. To study the effect of spatial resolution on MACD results, two sets of images were reconstructed. The first set utilized all acquired k-space data, achieving a resolution of $0.31 \times 0.31\ mm^2$. In contrast, the second set zero-filled 40% of the acquired outer k-space along the phase encoding direction, resulting in an acquired voxel size of $0.31 \times 0.52\ mm^2$. From the reconstructed images, phase difference and magnitude images were calculated using Eq. (11) and root mean square of coil magnitude images, respectively.

The complex difference images were calculated using Eq. (10) from the phase difference and magnitude images after detrending. Equation (10) was used for complex difference image calculation as no phase oscillations were observed in I_{off}. Ring-shaped background ROI were defined which had inner and outer radii of 1.6 mm and 3.4 mm, respectively. The tube center was determined as the brightest voxel in the magnitude image. The MACD analysis was performed for voxels within a circular ROI with a radius of 0.047 mm (3 voxels) centered at the tube. Since water is a Newtonian fluid, we assumed a laminar velocity profile as given by Eq. (1). The procedures of nonlinear fitting were identical to that in the Simulation section. Signal intensity in the background ROI was used for obtaining the scaling factor A using Eq. (5), with WM T_1 and T_2^* replaced by those of tap water. As both the vessel and background contained tap water, $\gamma = 1$ and the T_2^* value has no effect on the model image. The water T_1 was obtained by fitting the standard longitudinal magnetization recovery equation to the signal versus TR curve in a circular ROI of 1-cm diameter outside the tube.

For comparison, apparent velocities (v_{appa}) without correcting for partial volume effects were also calculated from the phase value (φ) of the voxel at the tube center in the detrended phase difference images as: $v_{appa} = \mathrm{VENC} \cdot \varphi/\pi$.

The means and SDs of v_{appa}, v_{mean}, D, and VFR obtained under the same scan and spatial resolution conditions were calculated and from which random and systematic errors were estimated as described in the Simulation section. To allow the comparison of random errors between the two spatial resolutions when their scan times are equal, SDs for the $0.31 \times 0.52\ mm^2$ results were normalized by $\sqrt{5/3}$ to compensate for the shorter acquisition time spent on acquiring only the central part of the k-space. Wilcoxon signed rank tests were performed to compare the MACD results estimated from the two spatial resolutions. For both phantom and *in vivo* results, a p value less than 0.05 was considered significant and Bonferroni correction was used to correct for multiple comparisons.

2.4. In vivo experiments

Two *in vivo* studies were carried out to (1) evaluate the reproducibility and voxel size dependence of MACD approach *in vivo* (reproducibility study), and (2) study the age dependence of the PA properties (age-dependence study). The studies were approved by the Institutional Review Board at University of North Carolina at Chapel Hill. Written informed consent was obtained from each subject before the MRI scans.

Subjects: 50 healthy volunteers without history of hypertension or neurological diseases participated in the study: 6 (ages: 21–41 yrs; 4 male) in Study 1, and 44 (ages 21–55 yrs; 12 male) in Study 2. The subjects in Study 2 were evenly distributed between 21 and 55 years old. The age range was chosen to allow investigating the age-dependent morphological changes of PA and surrounding PVS in relatively young and healthy subjects. The results for the PVS study will be published separately.

Table 2
MRI sequence parameters for phantom and *in vivo* studies.

Sequence	Phantom				In vivo			
	PC MRI	3D GRE	Variable-TR TSE	B1 map	PC MRI (Study 1)	PC MRI (Study 2)	3D TSE	B1 map
TE (ms)	15.7	2.38	12	1.89	15.7	15.7	328	1.89
TR (ms)	30.0	6.6	280 – 18000	15000	25.5–30.0	30.0	3000	8000
VENC (cm/s)	4	N/A	N/A	N/A	4	4	N/A	N/A
FOV (mm^2)	200 × 162.5	100 × 100 × 64	220 × 220	120 × 120	200 × 162.5	200 × 162.5	210 × 210 × 99.2	200 × 200
Resolution (mm^2)	0.31 × 0.31	0.52 × 0.52	1.7 × 1.7	1.9 × 1.9	0.31 × 0.31	0.31 × 0.52	0.41 × 0.41	3.1 × 3.1
Slice thickness (mm)	2	0.5	5	5	2	2	0.40	5
Matrix Size	640 × 520	192 × 192	128 × 128	64 × 64	640 × 520	640 × 312	512 × 512	64 × 64
Slices	1	128	1	8	1	1	248	16
FA (degree)	45	4	90	8	30, 45, or 60	45	variable	8
BW (Hz/pix)	78	310	130	490	78	78	376	490
GRAPPA factor	1	2	1	1	2	2	3	1
Averages	5	1	1	1	15–20	20	1	1
Scan time (min)	2:37	1:30	11:56	0:30	3:36–4:59	3:26	8:03	0:16

Data acquisition: The PC MRI sequence was identical to that used for the phantom study. The imaging parameters are given in the 6th and 7th columns of Table 2. The scan time was comparable to those in a recent study (Geurts et al., 2018a). We acquired a single axial slice at 1.5 cm above the corpus callosum. In Study 1, the slice location and voxel size matched with those suggested in a recent study (Geurts et al., 2018a). Large FAs (i.e. > Ernst angle) were chosen to increase in-flow signal enhancement and suppress white matter signal. Three FAs were used and were found to produce similar numbers of PAs in WM. Therefore, their results were combined in group analysis. To evaluate reproducibility, scans were performed twice during the same session with identical parameters. In Study 2, the sequence parameters matched closely with those in Study 1, except for a lower spatial resolution of $0.3125 \times 0.5208\,mm^2$. In addition to acquiring images at 1.5 cm above the corpus callosum, a second slice 0.4 cm inferior to the first slice was acquired in a subset of subjects (n = 29). The second slice was used to study the position dependence of the measured PA properties. To determine the PA orientation relative to the imaging slice, subjects were also scanned with a T_2-weighted 3D variable flip angle TSE sequence to visualize the PVSs surrounding the PAs (Bouvy et al., 2014; Zong et al., 2016), assuming that the PA and surrounding PVS have the same orientation. B_1 maps were acquired to achieve the desired FA in the CSO region. Parameters for the TSE and B_1 mapping sequences are given in the last two columns of Table 2.

Data analysis: The phase difference and magnitude images were reconstructed to a voxel size of $0.1563 \times 0.1563\,mm^2$. To study the effects of voxel size for *in vivo* MACD results, image resolution in Study 1 was reduced to $0.31 \times 0.52\,mm^2$ using the identical method described for the phantom images. PAs were automatically delineated from the phase difference and magnitude images with the original spatial resolution of $0.31 \times 0.31\,mm^2$ using a threshold based method, as described in the supplementary materials. The orientations of delineated PAs were determined from those of matched PVSs automatically segmented from the 3D TSE images (Lian et al., 2018). The details of PVS orientation determination can also be found in the supplementary materials, where we estimated the uncertainty for PVS orientation to be about 6°.

MACD analyses were only performed on PAs that can be matched with PVSs such that their tilt angles could be determined and was found to be 0°. The procedures for complex difference image calculation and fitting were the same as in the phantom study, except that the blunted parabolic velocity profile was assumed. The PA positions were estimated from the center of mass of each PA cluster. The inner and outer radii of the ring-shaped background ROI were 0.94 mm and 1.72 mm, respectively, while the radius of the PA ROI for fitting was 0.47 mm. γ and blood and WM T_1 and T_2* values were the same as those listed in Table 1. As early studies have reported PA diameters in the range of 40–536 μm in the basal ganglia, PAs with fitted diameters greater than 536 μm were considered outliers and excluded from analysis (Fisher, 1968; Pesce and Carli, 1988). Such outliers accounted for 2.7% of all perpendicular PAs analyzed.

For the reproducibility study, PAs that were detected in the first scan were matched to those in the second scan in the same subject if their centers of mass were separated by less than 2 mm. PAs that were separated by more than 2 mm in the two scans were assumed to be different PAs. Those matched PAs were then used for generating Bland-Altman plots and estimating the coefficients of repeatability (CR) of the fitted v_{mean}, D, and VFR. To compare the *in vivo* CR with simulation results, the simulated SD versus true D and true v_{mean} results were interpolated to the measured mean v_{mean} and D, which was then multiplied by $1.96\sqrt{2}$ to obtain simulated CRs for comparison.

Group means and SDs of the number of delineated PAs (N_{PA}) were calculated. Means and SDs of the fitted D, v_{mean}, and VFR over all perpendicular vessels in all subjects were also calculated. Because of the different N_{PA} in the subjects, all statistical analyses in D, v_{mean}, and VFR were performed over vessels without first averaging within each subject, except for the comparison of the MACD results of the superior and inferior slices and for Fig. 9(B)–(D) where, for clarity, means and SDs over PAs within each subject were plotted. The same statistical tests as in the phantom study were performed to compare the MACD results between the two spatial resolutions in Study 1. Spearman's correlation and linear regression analysis were performed to study the relationship between the vessel properties and age. 95% confident intervals for the slopes of the changes in the vessel properties with age were calculated from the linear regression.

2.5. Data and code availability statement

The MRI images and Matlab codes for simulation and performing MACD analysis are available in Mendeley Data (https://doi.org/10.17632/8bsgw4rhtr.1).

3. Results

3.1. Simulation

In our study, a five lobe sinc pulse apodized with a Hamming window was employed. The SS profile η(z) obtained via Bloch simulation is shown in Fig. 1(C). The corresponding normalized $M_{\perp}^{t}(v)$ is shown in Fig. 1(B), assuming blood $T_1 = 2.6$ s and TR = 26 ms. For comparison, the normalized $M_{\perp}^{t}(v)$ for an ideal pulse with a boxcar SS profile identical to that assumed by Hoogeveen et al. are also shown (Hoogeveen et al., 1999). It is clear from Fig. 1(B) that $M_{\perp}^{t}(v)$ depends strongly on the SS profile. Therefore, the $M_{\perp}^{t}(v)$ curve for the apodized sinc pulse was employed for the simulation and analysis of phantom and *in vivo* images.

Fig. 3(A), (C), and (E) show the random errors of the MACD and MAP results simulated at different true v_{mean} and PVF. The random errors increased with decreasing true v_{mean} and PVF. Furthermore, the random errors of the MACD results were much smaller than those of MAP. For example, for a vessel with PVF = 0.2 (D = 0.16 mm) and flow velocity of 1 cm/s, the random errors of v_{mean} and D for MACD were 0.12 cm/s and 0.016 mm, respectively, whereas the corresponding errors were 0.44 cm/s and 0.061 mm, respectively, with the MAP approach.

Noise-induced systematic errors of the fitted v_{mean}, D, and VFR are shown in Fig. 3 (B), (D), and (F). The systematic errors were lower with the MACD approach than MAP. The errors were generally larger at lower true v_{mean} and D but also increased when the true v_{mean} and PVF approached 2 cm/s and 1, respectively. However, all systematic errors for MACD were ≤3% of the true parameter values when true $v_{mean} \geq 0.8$ cm/s and PVF≥0.2.

Fig. 4 shows the dependence of noise-related MACD errors on noise levels (1/SNR). The random errors were approximately proportional to the noise level in all cases. Furthermore, the systematic errors were negligible when SNR≥15. At lower SNR, non-zero systematic errors were observed, consistent with the results shown in Fig. 3.

Systematic errors in fitted v_{mean}, D, and VFR caused by errors of assumed blood and WM T_1 and T_2*, FA, and γ in calculating model image are shown in Fig. 5. v_{mean} was almost independent of the model parameter errors, while D varied linearly with WM T_1, WM T_2^*, blood T_2^*, and γ. D was almost independent of the true blood T_1 and exhibited a nonlinear dependence on true FA. In all cases, the maximum diameter error was ≤10%, when the errors in model parameters were 20%. When the true velocity profile was laminar instead of the assumed blunted parabolic flow, the systematic errors for fitted v_{mean}, D, and VFR were 25%, −13%, and −5%, respectively.

3.2. Phantom study

A water T_1 of 3.02 ± 0.16 s was measured using the variable-TR TSE sequence and was used for calculating the model images for MACD analysis. Consistent with simulation, the random errors of the MACD

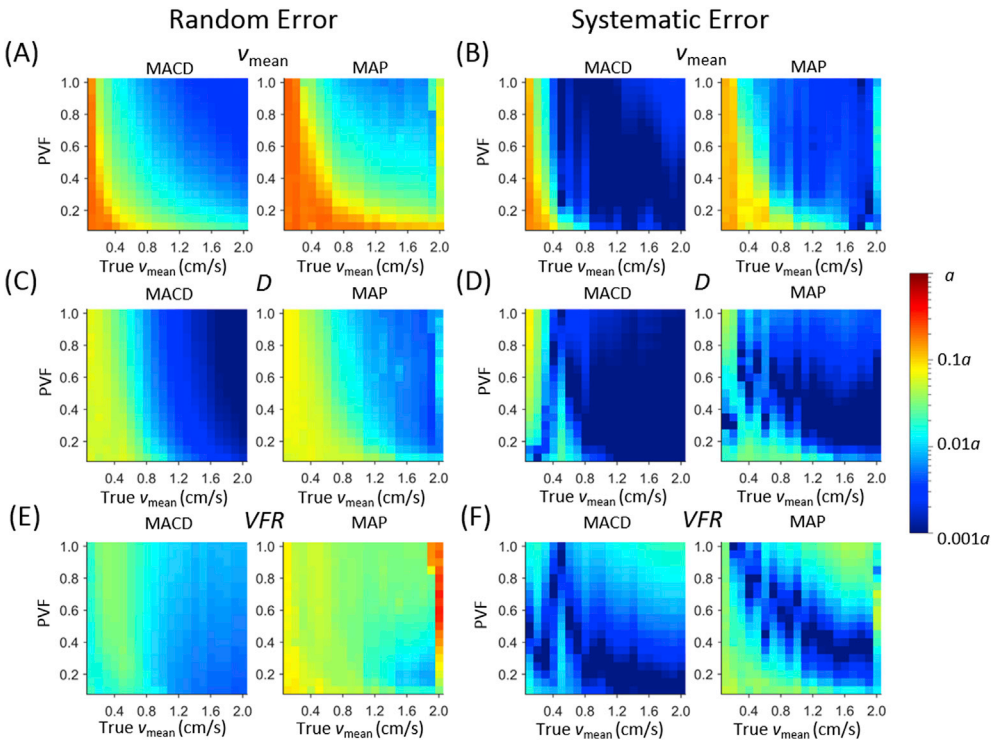

Fig. 3. Color maps of the random ((A), (C), (E)) and systematic errors ((B), (D), (F)) of the fitted v_{mean}, *D*, and VFR in the simulation as a function of true v_{mean} and partial volume fraction. The left and right images in each panel correspond to MACD and MAP results, respectively. A log scale was used in the color maps to accommodate the large range of values. The parameter *a* in the color bar is equal to 5 cm/s, 2 mm, and 2 mm^3/s for v_{mean}, *D*, and VFR, respectively. Overall, the MACD method yields smaller standard deviations and systematic errors than MAP.

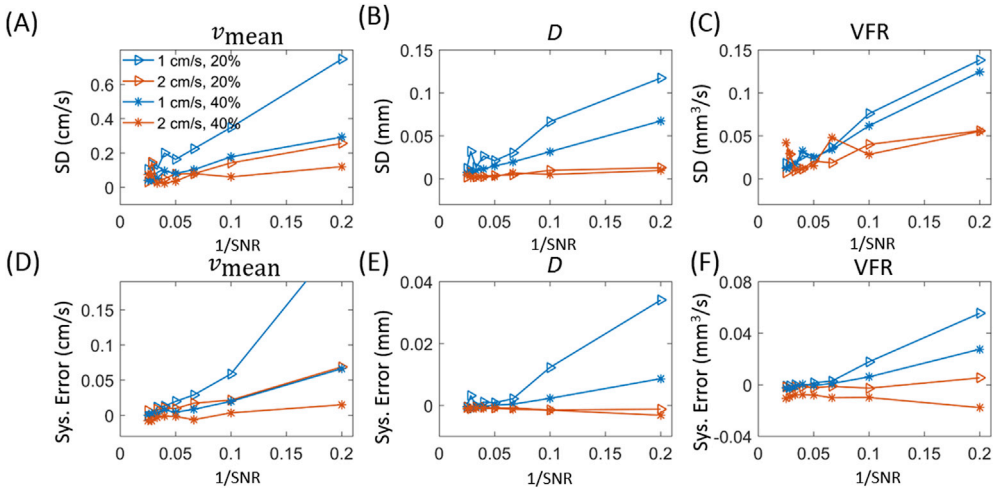

Fig. 4. Dependences on the white matter SNR of the (A–C) random and (D–F) systematic errors of MACD results. Different symbols correspond to different combinations of true v_{mean} (1 and 2 cm/s) and PVF (20% and 40%), respectively. As expected, the errors increase at lower SNR.

results increased monotonically with decreased velocity (Fig. 6(A) – (C)). The errors were similar between the two voxel sizes.

Without correcting for partial volume effects, the v_{appa} underestimated the true velocities by 0.24–0.33 cm/s (19%–38%) and 0.43–0.61 cm/s (36%–54%) for voxel size of $0.31 \times 0.31\ mm^2$ and $0.31 \times 0.52\ mm^2$, respectively. After the correction with MACD, the absolute differences between the measured and true v_{mean} were reduced to 0.02–0.14 cm/s (2%–9%) and 0.001–0.09 cm/s (0.1%–6%) for these two voxel sizes, respectively, for $v_{mean} \geq 1$ cm/s (Fig. 6(D)). In addition to correcting for v_{mean} errors, MACD-derived *D* and VFRs also agreed well with the true values at $v_{mean} \geq 1$ cm/s, as shown in Fig. 6(E) and (F), where their errors were 0.001–0.016 mm (0.5%–11%) and 0.003–0.05 mm^3/s (1%–20%), respectively. However, the errors became larger for v_{mean} and *D* and reached 19% and 31%, respectively, at a lower v_{mean} of 0.8 cm/s.

The differences in v_{mean}, *D*, and VFR between the two voxel sizes were not significant (p-values ≥ 0.07) at all four v_{mean} except for VFR at true v_{mean} of 1.25 cm/s ($p = 0.0054$) and 1.5 cm/s ($p = 0.023$). However, both values were not statistically significant after Bonferroni correction.

The errors of v_{mean}, *D*, and VFR depended linearly on the tilt angle of the vessel when the angle was $\leq 2^\circ$ (Fig. 6(G) – (I)). When the angle was greater than 2°, the angular dependences became much weaker. On the other hand, v_{appa} remained relatively stable over the whole tilt angle range. The *D* and VFR errors were independent of voxel size when the angle was $\leq 2^\circ$ but became strongly voxel-size dependent above 2°.

3.3. *In vivo study*

3.3.1. *Reproducibility study*

Representative magnitude and phase difference images from Study 1

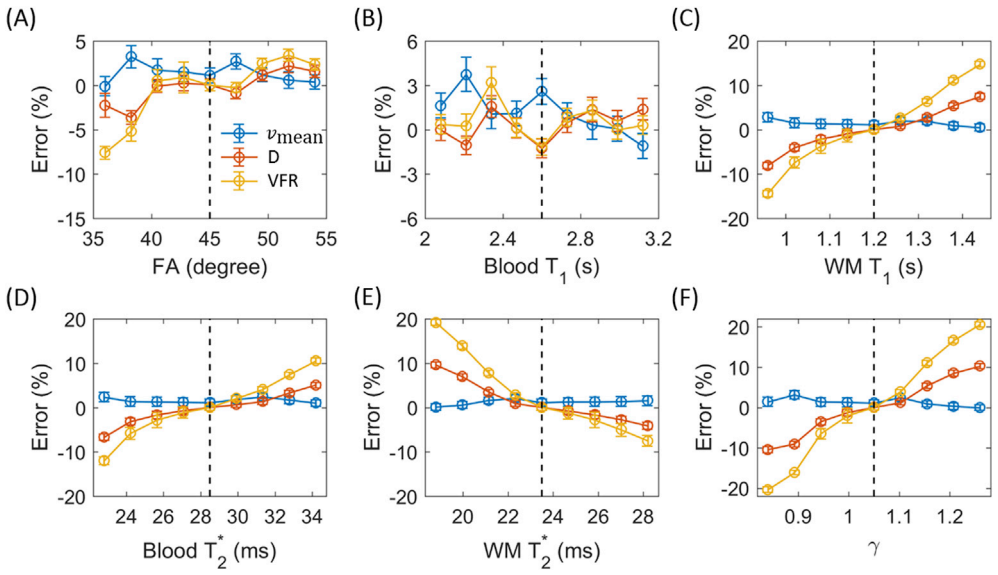

Fig. 5. Systematic errors of MACD results as a function of errors in one of the six model parameters. The parameter for each plot is shown below the horizontal axis. The v_{mean}, D, and VFR errors are normalized to the true v_{mean}, D, and VFR values, respectively. Each model parameter varies in the range of 80–120% of its true value denoted by the vertical dashed line. The assumed true v_{mean} and D were 1 cm/s and 0.158 mm, respectively.

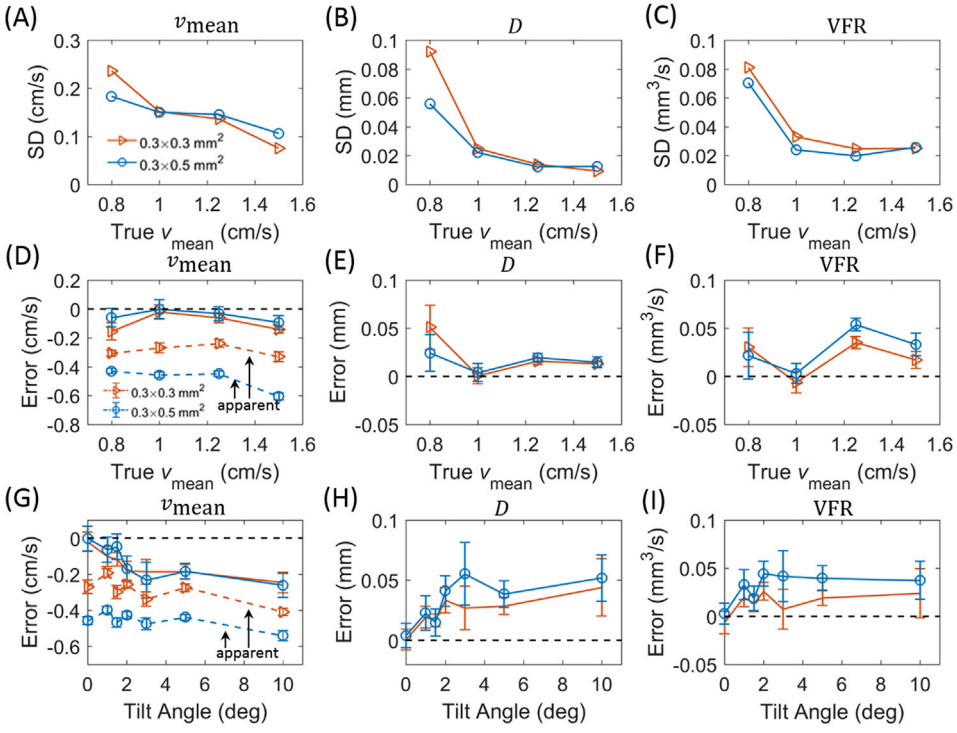

Fig. 6. (A)–(C) random and (D)–(F) systematic errors of the MACD results in the flow phantom at different true v_{mean}. (G)–(I) systematic errors at different tilt angles of the tube relative to the slice normal direction. The two colors represent the two different voxel sizes. For comparison, the differences between the apparent and true v_{mean} are also shown in (D) and (G) as dashed lines. The random errors for the blue lines in (A)–(C) are divided by $\sqrt{5/3}$ to account for the shorter scan times at lower resolution.

are shown in Fig. 7(A) – (C), where the red circles denote the penetrating arteries. The average number of delineated PAs over all scans were 27 ± 9 (mean and SD; $N = 12$; 6 subjects × 2 scans/subject), of which 18 ± 10 can be identified in the repeated images acquired from same subjects. Furthermore, among the vessels identified in both images, 6 ± 3 can be matched with a segmented PVS from the T_2-weighted images to determine the orientations of the vessels. Among the matched vessels, 4 ± 3 were perpendicular to the imaging plane and were analyzed with MACD. The v_{mean}, D, and VFR averaged over those vessels and their CRs are given in the second and third rows of Table 3, for spatial resolutions of $0.3 \times 0.3\,mm^2$ and $0.3 \times 0.5\,mm^2$, respectively. The Bland-Altman plots of v_{mean}, D, and VFR are shown in Fig. 8. The CRs for v_{mean}, D, and VFR at $0.3 \times 0.3\,mm^2$ were 195%, 328%, and 136% greater than the corresponding CRs interpolated from the simulated SDs at $v_{mean} = 1.6$ cm/s and $D = 0.14$ mm.

The Wilcoxon's signed rank test showed a significant difference in v_{mean} ($p = 2.5 \times 10^{-5}$) and VFR ($p = 4.2 \times 10^{-5}$) between the two voxel sizes, but no significant difference in D ($p = 0.65$). The differences in v_{mean} and VFR remained significant after Bonferroni correction.

3.3.2. *Age-dependence study*

We observed no significant age effect in the number of PAs (N_{PA}) or the PA properties, as shown in Fig. 9(A)–(D) for PAs in the superior slice. The average number of detected PAs in the slices was 33 ± 17, among which

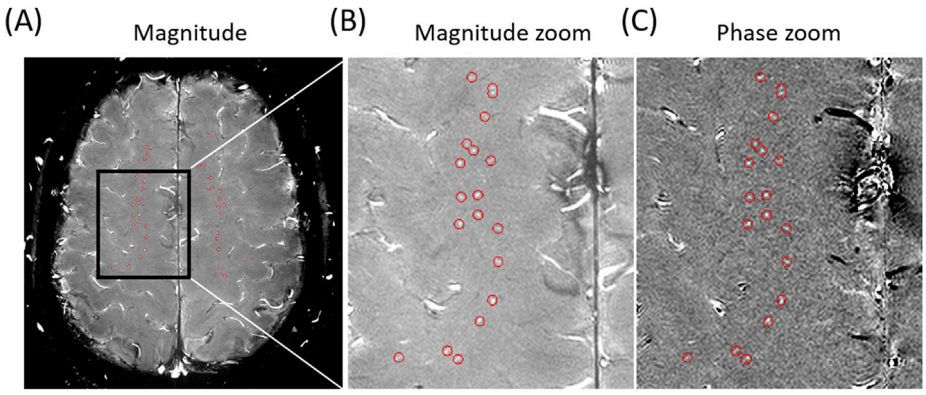

Fig. 7. (A) A representative PC MRI magnitude image with velocity encoding gradient off. (B) and (C) are magnified magnitude and PD images, respectively, of the region enclosed by the rectangle in (A). Red circles enclose PAs identified by the thresholding method.

Table 3
Means (columns 3–5) and coefficients of repeatability (columns 6–8) of *in vivo* v_{mean}, D, and VFR results. The numbers in the parentheses are standard deviations in columns 3–5 and CRs relative to the mean values in columns 6–8.

	Voxel Size (mm^2)	v_{mean} (cm/s)	D (mm)	VFR (mm^3/s)	CR of v_{mean} (cm/s)	CR of D (mm)	CR of VRF (mm^3/s)
Reproducibility Study	0.3×0.3	1.6 (0.5)	0.14 (0.02)	0.25 (0.07)	0.67 (42%)	0.06 (42%)	0.067 (27%)
	$0.3 \times 0.5\,mm^2$	1.8 (0.5)	0.15 (0.02)	0.31 (0.10)	0.73 (40%)	0.052 (35%)	0.12 (39%)
Age-dependence study	$0.3 \times 0.5\,mm^2$ (superior)	1.79 (0.62)	0.17 (0.05)	0.37 (0.18)	N/A	N/A	N/A
	$0.3 \times 0.5\,mm^2$ (inferior)	1.72 (0.61)	0.17 (0.05)	0.40 (0.23)	N/A	N/A	N/A

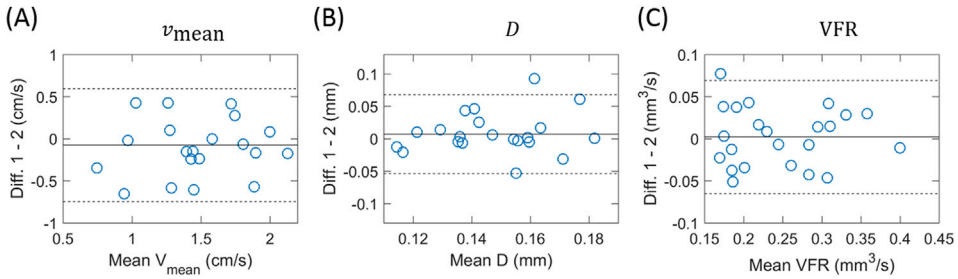

Fig. 8. Bland-Altman plots of the (A) v_{mean}, (B) D, and (C) VFR differences between the two scans in the *in vivo* Study 1. The values for the horizontal axes are means over the two scans. Each symbol corresponds to one perpendicular PA matched in the images of the two scans. The dashed lines are ±1.96 SD (SD of inter-scan difference) away from the mean value.

9 ± 6 ($30\% \pm 15\%$) could be matched with a PVS in 3D T_2–weighted images and 6 ± 5 ($19\% \pm 13\%$) were perpendicular to the imaging slice. To avoid errors due to vessel tilt, the v_{mean}, D, and VFR in Fig. 9(B)–(D) only included vessels that were perpendicular to the imaging plane. Only 31 subjects were included in these figures as five subjects were excluded due to the presence of severe motion artifacts in the images and no perpendicular vessels were found in another 8 subjects. The Spearman's correlation coefficients between age and N_{PA}, v_{mean}, D, and VFR were not significantly different from zero ($p \geq 0.56$). Linear regression of the four parameters versus age gave 95% confidence intervals for their slopes of [-0.25 0.17] yr^{-1}, [-0.006,0.010] cm/s/yr, [-0.0003,0.0010] mm/yr, and [-0.0012,0.0037] $mm^3/s/yr$, respectively. As no age effects were observed, mean results averaged over the perpendicular vessels in all subjects were also calculated. The resulting mean v_{mean}, D, and VFR are given in the fourth rows of Table 3, in good agreement with results of Study 1 at the same spatial resolution (second row in Table 3).

In the subset of 29 subjects with a second more inferior slice, four were excluded due to motion and another five were excluded due to a lack of perpendicular vessels. No significant difference was observed in the N_{PA}, v_{mean}, D, or VFR between the two slice locations. The Wilcoxon signed rank test of the intra-subject inter-slice difference in N_{PA}, mean v_{mean}, D, or VFR over all perpendicular vessels in the slice was not significant ($p \geq 0.63$). The mean v_{mean}, D, and VFR over the 20 subjects are given in the fifth row of Table 3.

4. Discussion

In this study, we carried out simulation, phantom, and *in vivo* studies to evaluate the proposed MACD approach for estimating v_{mean}, D, and VFR from phase contrast MRI. According to our simulation results (Fig. 3), the MACD method offers an improved precision and accuracy when compared to an earlier method utilizing only phase images (Hoogeveen et al., 1999), enabling quantitative characterization of PA properties in the presence of severe partial volume effects. The improvements of MACD method over MAP can be explained by several factors. First, the number of data points for the model fitting is doubled in MACD. Second, a more accurate modeling of flow-induced signal enhancement is performed. Finally, v_{mean} and D are sensitive to different information in the complex difference images, as explained in the Theory section.

Our simulation at different noise levels suggests that under *in vivo* conditions, i.e. WM SNR ~27, the random errors of the fitted v_{mean}, D, and VFR increase linearly with noise, while there are almost no systemic errors at SNR≥10(Fig. 4). Therefore, it is preferable to acquire multiple short ~3 min scans as in the current study to reduce measurement errors. With a longer scan, head motion could lead to image blurring and offset the SNR gain, resulting in less accurate results (Geurts et al., 2018a).

The application of the MACD approach requires determination of FA, blood T_2^*, T_1 and the scaling factor A, which depends on three WM tissue properties (i.e. $T_{2,wm}^*$, $T_{1,wm}$, and γ). Our simulation (Fig. 5) shows that

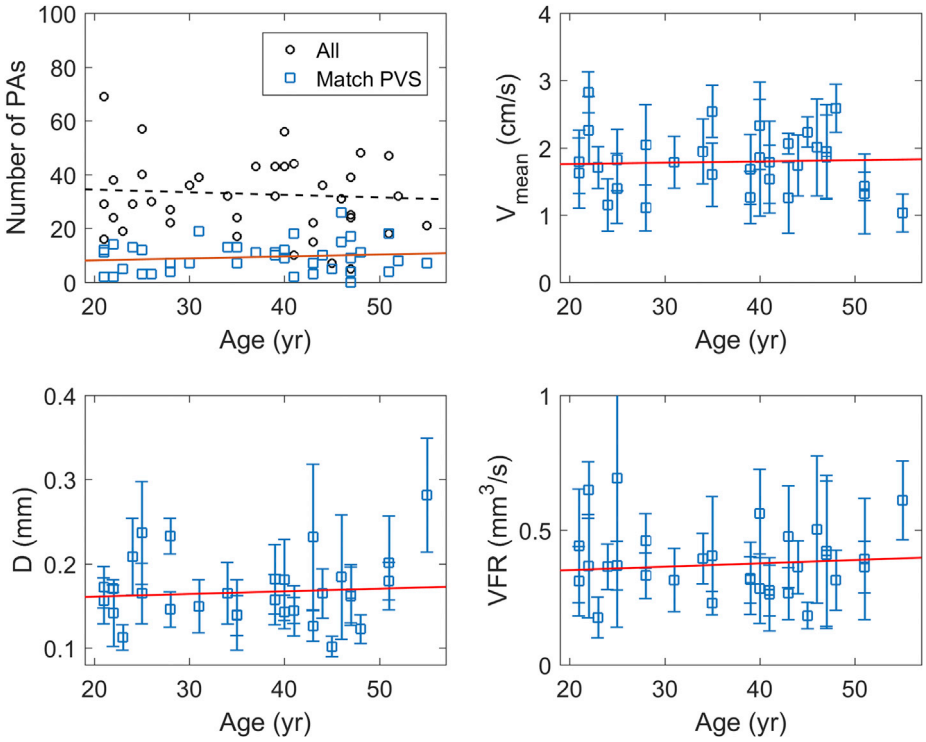

Fig. 9. (A) Number of detected PAs, (B) v_{mean}, (C) D, and (D) VFR in different subjects versus their ages in the superior slices that were 1.5 cm above CC. In (A), the black circles represent all PAs detected by the thresholding algorithm while the blue squares are those that could be matched with PVSs. In (B)–(D), the symbols and error bars represent the means and SDs over all perpendicular PAs in a subject, respectively. The lines are least square linear fits.

errors in those parameters in general result in smaller percent errors in the PA parameters, especially for v_{mean} and D. It is interesting to note that v_{mean} is not sensitive to errors in those parameters, which can be explained by the fact that v_{mean} is determined mostly from the phase of the complex difference image, while the six parameters only affect the magnitude of the model images. Since these parameters can be altered under diseased conditions, their values should be measured to ensure accuracy of the D and VFR results.

In both the simulation and phantom studies, the random errors increase at a lower velocity, which can be explained by smaller flow enhancement and thus lower SNR. It is interesting to note that in the phantom study, despite the decreased PVF with retrospectively downsampled images, the accuracy and precision of the MACD results are similar to those obtained from the original higher resolution images. Nevertheless, the apparent velocities differ greatly between the two resolutions, suggesting that the partial volume effects are properly modeled in the MACD approach. Due to the small sizes of the vessels, its spectral density extends well beyond the boundaries of the sampled k-spaces and only the relatively flat low frequency components are sampled at both resolutions. Therefore, the scan time normalized SNR of the complex difference images are similar at the two spatial resolutions, which explained the similar random errors of the MACD results (Fig. 6(A)-(C)) between the two resolutions.

The measurement of angular dependence of MACD results found a strong effect of the tilt angle (α) at $\alpha \leq 2^{\circ}$. The reason for the strong angular dependence is unclear. The flow-induced phase shift should have cosα dependence on the angle, which has a quadratic angular dependence. The angular dependence may be related to the misalignment of the vessel cross sections within the imaging slice which instead has a tanα dependence. More study is needed to understand the origin of the strong angular dependence and develop methods to correct for the angular effects.

We further obtained the CRs of *in vivo* MACD results, which were 176%–338% higher than estimated from simulation. In addition to the presence of random noises, *in vivo* images can also suffer from head motion induced artifacts. In the future, prospective motion correction techniques may be incorporated to reduce motion artifacts, which can in turn reduce CR (Gallichan et al., 2016).

We note that although the measured vessel properties were not significantly different between voxel sizes of $0.31 \times 0.31\,mm^2$ and $0.31 \times 0.52\,mm^2$ in the flow phantom, this finding differs from *in vivo* results. In Study 1, the v_{mean} for $0.31 \times 0.52\,mm^2$ was ~0.2 cm/s (13%) higher than that at $0.31 \times 0.31\,mm^2$, while D is similar between the two voxel sizes. The reason underlying the discrepancy remains unknown. The potential tilt of the PAs can not explain the observed results since it would cause stronger voxel size dependence in D than in v_{mean}, as shown in Fig. 6(G) and (H). Other possible reasons such as presence of PA curvature need to be explored in future studies.

We found no significant age-dependent changes in PA properties in 31 neurologically normal subjects with ages ranging between 21 and 55 years. In a recent study (Geurts et al., 2018a), no significant differences in apparent velocity and number of PAs were observed between young (mean age 26 yrs) and old age groups (mean age 63 yrs), consistent with our results. Other studies focusing on the internal carotid arteries reported small diameter increases of ~6%–12% between subjects of 21–30 and 51–60 years old (Jeon et al., 2018; Kamenskiy et al., 2015). Similar small changes in PA diameters are unlikely to be detected in the current study and fall within the 95% confidence interval of the change rate of D with age.

The PA properties measured in healthy subjects in this study may serve as normative values for studying pathologically induced PA changes in SVD and other neurological diseases. In SVD, both narrowing of PA lumen and leakage of the blood brain barrier have been implicated as important contributing factors in the pathogenesis of the disease (Fisher, 1968; van Swieten et al., 1991; Wardlaw et al., 2001). The MACD method proposed in this study can be applied to evaluate whether or not lumen narrowing is present in patients. Furthermore, reduced cerebral blood flow in the WM has been reported in SVD patients (Bernbaum et al., 2015; Yao et al., 1992). Quantitative measurements of PAs with MACD can potentially reveal whether CBF reduction is associated with reduced velocity in PAs alone, suggesting increased resistance due to

reduction of capillary density (Joutel et al., 2010), or narrowing of PA lumen, or both. In addition, vascular reactivity measurement with hypercapnic challenge is a promising technique for assessing the functional integrity of the PAs in SVD (Geurts et al., 2018b). Our MACD analysis approach may help determine whether the apparent velocity increase in response to hypercapnic challenge is due to velocity increase alone which may be passively induced by increased velocity of upstream vessels, or due to active PA dilations.

There are several limitations of the proposed MACD approach. First, the MACD results depend strongly on the orientation of the PAs relative to the slice normal direction. Since it is challenging to achieve high accuracy (error $< 1°$) for determining PA orientations for *in vivo* studies, the orientation dependence will introduce additional uncertainties to the MACD results. Second, the MACD approach approximates the blood vessels as straight cylinders, which does not hold for tortuous vessels that may occur inside enlarged PVSs (Brown et al., 2002). Third, in addition to PA orientation, the accuracy of the MACD results also relies on the assumptions of the flow pattern and the values of six parameters in Table 1. For applications to diseased populations, it is important to evaluate the potential changes of the parameters due to the diseases. Last, the PC-MRI sequence can only visualize a small fraction of the PAs in CSO with diameters above 0.1 mm. Therefore, there exists a sampling bias in the quantified PAs, which might also have contributed to the lack of any age effects observed in this study.

5. Conclusions

We have developed a new MACD approach for quantitative measurement of v_{mean}, diameter, and VFR of penetrating arteries in CSO in the presence of severe partial volume effects. Our simulation demonstrates that MACD results have smaller random and systematic errors when compared to MAP. Our phantom study revealed increased random errors at lower velocity, in agreement with simulation. Tilt angle between vessel and slice normal direction has a strong effect on the accuracy of MACD results. When there is negligible tilt, accurate measurements of v_{mean}, *D,* and VFR were achieved with relative errors $\leq$20% at $v_{mean} \geq 1$ cm/s. *In vivo* PA diameters and velocities and their age dependences were measured for the first time in the CSO of healthy human subjects. No significant age effects were observed in healthy subjects between ages of 21–55 yrs. The proposed MACD method may serve as a useful tool for investigating pathological PA changes in small vessel disease.

Acknowledgements

This study was supported by NIH grant 5R21NS095027-02. We thank the reviewers for their constructive comments, Study Coordinator Jordan Jimenez for her support, Dr. Heather Decot for proofreading the manuscript, and Dr. Chunfeng Liang for segmenting the PVS masks.

Appendix A. Supplementary data

Supplementary data to this article can be found online at https://doi.org/10.1016/j.neuroimage.2019.03.059.

Appendix

In the following, the equations for numerically calculating $M_{\perp}^{t}$ and $M_{\perp,wm}^{t}$ will be described.

In the presence of flow perpendicular to the slice, spins at position z immediately prior to a RF pulse is at position $z - v \cdot \mathrm{TR}$ at the corresponding time of the previous TR. Therefore, assuming a steady state and that the transverse magnetization is completely spoiled after readout, the longitudinal magnetization M_z at these two locations are related to each other via the following equation:

$$M_z(v,z) = 1 - [1 - M_z(v, z - v \cdot TR) \cdot \cos(FA \cdot \eta(z - v \cdot TR))] \cdot \exp(-TR/T_{1,b}), \tag{A1}$$

where $T_{1,b}$ is the blood T_1, and FA the flip angle, and $\eta(z)$ the normalized RF slice selection profile. $M_z(v,z)$ can be calculated iteratively from Eq. (A1) until reaching sufficiently large iteration numbers (n) for which $\eta(z - n\mathrm{TR} \cdot v) = 0$ and $M_z(v, z - n\mathrm{TR} \cdot v) = 1$. The total transverse magnetization ($M_{\perp}^{t}$) at a given location (x, y) is a function of its velocity $v(x,y)$ and is given by an integration of $M_{\perp}(v,z)$ along z:

$$M_{\perp}^{t}(v) = \int_{-\infty}^{\infty} M_{\perp}(v,z)dz = \exp\left(-TE/T_{2,b}^{*}\right) \cdot \int_{-\infty}^{\infty} M_z(v,z)\sin(FA \cdot \eta(z))dz, \tag{A2}$$

where TE is the echo time, and $T_{2,b}^{*}$ is the blood T_2^{*}. During model fitting and simulation, the $M_{\perp}^{t}$ versus v curve can be pre-calculated prior to calculating the convolutions and used to interpolate $M_{\perp}^{t}$ at arbitrary v at the positions of the elements for calculating convolution.

For WM, we have $v = 0$ and an analytical expression can be obtained for $M_z(v,z)$ from Eq. (A1), resulting in the following equation for the total WM transverse magnetization:

$$M_{\perp,wm}^{t} = \exp\left(-TE/T_{2,wm}^{*}\right) \cdot \int_{-\infty}^{\infty} \frac{[1 - \exp(-TR/T_{1,wm})]\sin(FA \cdot \eta(z))}{1 - \cos(FA \cdot \eta(z)) \cdot \exp(-TR/T_{1,wm})} dz, \tag{A3}$$

where $T_{1,wm}$ and $T_{2,wm}^{*}$ are the WM T_1 and T_2^{*}.

References

Bernbaum, M., Menon, B.K., Fick, G., Smith, E.E., Goyal, M., Frayne, R., Coutts, S.B., 2015. Reduced blood flow in normal white matter predicts development of leukoaraiosis. J. Cereb. Blood Flow Metab. 35, 1610–1615.

Bernstein, M.A., Grgic, M., Brosnan, T.J., Pelc, N.J., 1994. Reconstructions of phase contrast, phased array multicoil data. Magn. Reson. Med. 32, 330–334.

Bouvy, W.H., Biessels, G.J., Kuijf, H.J., Kappelle, L.J., Luijten, P.R., Zwanenburg, J.J., 2014. Visualization of perivascular spaces and perforating arteries with 7 T magnetic resonance imaging. Investig. Radiol. 49, 307–313.

Bouvy, W.H., Geurts, L.J., Kuijf, H.J., Luijten, P.R., Kappelle, L.J., Biessels, G.J., Zwanenburg, J.J., 2016. Assessment of blood flow velocity and pulsatility in cerebral perforating arteries with 7-T quantitative flow MRI. NMR Biomed. 29, 1295–1304.

Brown, W.R., Moody, D.M., Challa, V.R., Thore, C.R., Anstrom, J.A., 2002. Venous collagenosis and arteriolar tortuosity in leukoaraiosis. J. Neurol. Sci. 203–204, 159–163.

Conturo, T.E., Beth, A.H., Arenstorf, R.F., Price, R.R., 1987. Simplified mathematical description of longitudinal recovery in multiple-echo sequences. Magn. Reson. Med. 4, 282–288.
Fisher, C.M., 1968. The arterial lesions underlying lacunes. Acta Neuropathol. 12, 1–15.
Furuta, A., Ishii, N., Nishihara, Y., Horie, A., 1991. Medullary arteries in aging and dementia. Stroke 22, 442–446.
Gallichan, D., Marques, J.P., Gruetter, R., 2016. Retrospective correction of involuntary microscopic head movement using highly accelerated fat image navigators (3D FatNavs) at 7T. Magn. Reson. Med. 75, 1030–1039.
Geurts, L., Biessels, G.J., Luijten, P., Zwanenburg, J., 2018a. Better and faster velocity pulsatility assessment in cerebral white matter perforating arteries with 7T quantitative flow MRI through improved slice profile, acquisition scheme, and postprocessing. Magn. Reson. Med. 79, 1473–1482.
Geurts, L.J., Bhogal, A.A., Siero, J.C.W., Luijten, P.R., Biessels, G.J., Zwanenburg, J.J.M., 2018b. Vascular reactivity in small cerebral perforating arteries with 7T phase contrast MRI - a proof of concept study. Neuroimage 172, 470–477.
Greenwood, J., Sandomire, M., 1950. Sampe size required for estimating the standard deviation as a percent of its true value. J. Am. Stat. Assoc. 45, 257–260.
Hamilton, C.A., 1994. Correction of partial volume inaccuracies in quantitative phase contrast MR angiography. Magn. Reson. Imaging 12, 1127–1130.
Herscovitch, P., Raichle, M.E., 1985. What is the correct value for the brain–blood partition coefficient for water? J. Cereb. Blood Flow Metab. 5, 65–69.
Hoogeveen, R.M., Bakker, C.J., Viergever, M.A., 1999. MR phase-contrast flow measurement with limited spatial resolution in small vessels: value of model-based image analysis. Magn. Reson. Med. 41, 520–528.
Jeon, S.J., Kwak, H.S., Chung, G.H., 2018. Widening and rotation of carotid artery with age: geometric approach. J. Stroke Cerebrovasc. Dis. 27, 865–870.
Jorgensen, D.R., Shaaban, C.E., Wiley, C.A., Gianaros, P.J., Mettenburg, J., Rosano, C., 2018. A population neuroscience approach to the study of cerebral small vessel disease in mid- and late-life: an Invited Review. Am. J. Physiol. Heart Circ. Physiol. 314, H1117–H1136.
Joutel, A., Monet-Lepretre, M., Gosele, C., Baron-Menguy, C., Hammes, A., Schmidt, S., Lemaire-Carrette, B., Domenga, V., Schedl, A., Lacombe, P., Hubner, N., 2010. Cerebrovascular dysfunction and microcirculation rarefaction precede white matter lesions in a mouse genetic model of cerebral ischemic small vessel disease. J. Clin. Investig. 120, 433–445.
Kamenskiy, A.V., Pipinos II, Carson, J.S., MacTaggart, J.N., Baxter, B.T., 2015. Age and disease-related geometric and structural remodeling of the carotid artery. J. Vasc. Surg. 62, 1521–1528.
Kang, C.K., Park, C.A., Lee, D.S., Lee, Y.B., Park, C.W., Kim, Y.B., Cho, Z.H., 2016. Velocity measurement of microvessels using phase-contrast magnetic resonance angiography at 7 Tesla MRI. Magn. Reson. Med. 75, 1640–1646.
Koutsiaris, A.G., 2009. A velocity profile equation for blood flow in small arterioles and venules of small mammals in vivo and an evaluation based on literature data. Clin. Hemorheol. Microcirc. 43, 321–334.
Lagerstrand, K.M., Lehmann, H., Starck, G., Vikhoff-Baaz, B., Ekholm, S., Forssell-Aronsson, E., 2002. Method to correct for the effects of limited spatial resolution in phase-contrast flow MRI measurements. Magn. Reson. Med. 48, 883–889.
Lian, C., Zhang, J., Liu, M., Zong, X., Hung, S.C., Lin, W., Shen, D., 2018. Multi-channel multi-scale fully convolutional network for 3D perivascular spaces segmentation in 7T MR images. Med. Image Anal. 46, 106–117.
Miao, Q., Paloneva, T., Tuominen, S., Poyhonen, M., Tuisku, S., Viitanen, M., Kalimo, H., 2004. Fibrosis and stenosis of the long penetrating cerebral arteries: the cause of the white matter pathology in cerebral autosomal dominant arteriopathy with subcortical infarcts and leukoencephalopathy. Brain Pathol. 14, 358–364.
Montagne, A., Nikolakopoulou, A.M., Zhao, Z., Sagare, A.P., Si, G., Lazic, D., Barnes, S.R., Daianu, M., Ramanathan, A., Go, A., Lawson, E.J., Wang, Y., Mack, W.J., Thompson, P.M., Schneider, J.A., Varkey, J., Langen, R., Mullins, E., Jacobs, R.E., Zlokovic, B.V., 2018. Pericyte degeneration causes white matter dysfunction in the mouse central nervous system. Nat. Med. 24, 326–337.
Nitz, W.R., Bradley Jr., W.G., Watanabe, A.S., Lee, R.R., Burgoyne, B., O'Sullivan, R.M., Herbst, M.D., 1992. Flow dynamics of cerebrospinal fluid: assessment with phase-contrast velocity MR imaging performed with retrospective cardiac gating. Radiology 183, 395–405.
Pantoni, L., 2010. Cerebral small vessel disease: from pathogenesis and clinical characteristics to therapeutic challenges. Lancet Neurol. 9, 689–701.
Pesce, C., Carli, F., 1988. Allometry of the perivascular spaces of the putamen in aging. Acta Neuropathol. 76, 292–294.
Rooney, W.D., Johnson, G., Li, X., Cohen, E.R., Kim, S.G., Ugurbil, K., Springer Jr., C.S., 2007. Magnetic field and tissue dependencies of human brain longitudinal 1H2O relaxation in vivo. Magn. Reson. Med. 57, 308–318.
Schnerr, R.S., Jansen, J.F.A., Uludag, K., Hofman, P.A.M., Wildberger, J.E., van Oostenbrugge, R.J., Backes, W.H., 2017. Pulsatility of lenticulostriate arteries assessed by 7 tesla flow MRI-measurement, reproducibility, and applicability to aging effect. Front. Physiol. 8, 961.
Snyder, H.M., Corriveau, R.A., Craft, S., Faber, J.E., Greenberg, S.M., Knopman, D., Lamb, B.T., Montine, T.J., Nedergaard, M., Schaffer, C.B., Schneider, J.A., Wellington, C., Wilcock, D.M., Zipfel, G.J., Zlokovic, B., Bain, L.J., Bosetti, F., Galis, Z.S., Koroshetz, W., Carrillo, M.C., 2015. Vascular contributions to cognitive impairment and dementia including Alzheimer's disease. Alzheimers Dement 11, 710–717.
Tang, C., Blatter, D.D., Parker, D.L., 1995. Correction of partial-volume effects in phase-contrast flow measurements. J. Magn. Reson. Imaging 5, 175–180.
ten Dam, V.H., van den Heuvel, D.M., de Craen, A.J., Bollen, E.L., Murray, H.M., Westendorp, R.G., Blauw, G.J., van Buchem, M.A., 2007. Decline in total cerebral blood flow is linked with increase in periventricular but not deep white matter hyperintensities. Radiology 243, 198–203.
van der Veen, P.H., Muller, M., Vincken, K.L., Hendrikse, J., Mali, W.P., van der Graaf, Y., Geerlings, M.I., Group, S.S., 2015. Longitudinal relationship between cerebral small-vessel disease and cerebral blood flow: the second manifestations of arterial disease-magnetic resonance study. Stroke 46, 1233–1238.
van Swieten, J.C., van den Hout, J.H., van Ketel, B.A., Hijdra, A., Wokke, J.H., van Gijn, J., 1991. Periventricular lesions in the white matter on magnetic resonance imaging in the elderly. A morphometric correlation with arteriolosclerosis and dilated perivascular spaces. Brain 114 (Pt 2), 761–774.
Wardlaw, J.M., Dennis, M.S., Warlow, C.P., Sandercock, P.A., 2001. Imaging appearance of the symptomatic perforating artery in patients with lacunar infarction: occlusion or other vascular pathology? Ann. Neurol. 50, 208–215.
Yao, H., Sadoshima, S., Ibayashi, S., Kuwabara, Y., Ichiya, Y., Fujishima, M., 1992. Leukoaraiosis and dementia in hypertensive patients. Stroke 23, 1673–1677.
Zong, X., Park, S.H., Shen, D., Lin, W., 2016. Visualization of perivascular spaces in the human brain at 7T: sequence optimization and morphology characterization. Neuroimage 125, 895–902.